Desalination and Water Treatment
www.deswater.com

doi: 10.5004/dwt.2022.28617

268 (2022) 36–47
August

Fabrication of porous biochar decorated with $MnFe_2O_4$ magnetic nanoparticle for high effective removal of Cr(VI) ion in solution

Jingjing Han[a,b], Renrong Liu[a], Huifang Wang[a], Muqing Qiu[a,*], Baowei Hu[a]

[a]*School of Life Science, Shaoxing University, Shaoxing 312000, China, email: qiumuqing@usx.edu.cn (M. Qiu)*
[b]*Zhejiang Shaoxing Ecological Environment Monitoring Center, Shaoxing 312000, China*

Received 16 February 2022; Accepted 3 June 2022

ABSTRACT

Heavy metals posed a very important treat to public health and environment because of their toxicity, bioaccumulation and biodegradability properties. The development of high efficiency, low cost and good chemical stability adsorbents for removing heavy metals from aqueous solution was very urgent. The removal capacity of Cr(VI) by the preparation of porous biochar decorated with $MnFe_2O_4$ magnetic nanoparticle ($MnFe_2O_4$@PS) was evaluated. Results showed that the operational parameters had an important influence on Cr(VI) removal. Pseudo-second-order model and Langmuir model could be used to describe the adsorption process. The adsorption process of Cr(VI) by $MnFe_2O_4$@PS composites was a spontaneous, endothermic and randomness process. The removal capacity of Cr(VI) by $MnFe_2O_4$@PS composites reached 46.51 mg/g. The main mechanisms contained electrostatic interaction, Surface adsorption, surface complexation and chemical precipitation. $MnFe_2O_4$@PS composites exhibited high removal capacity of Cr(VI), good chemical stability and recyclability.

Keywords: Biochar; $MnFe_2O_4$ magnetic nanoparticle; Removal; Cr(VI)

1. Introduction

With the rapid development of industrialization as well as urbanization, heavy metals posed a very important treat to public health and environment because of their toxicity, bioaccumulation and biodegradability properties [1,2]. They were discharged into the environment through mining, electroplating, leather industries, anodizing bath, wood preservation, and so on [3]. Among them, chromium was considered as one of the hazardous heavy metal. The World Health Organization reported that the maximum contaminant level for concentration of chromium in drinking water was 0.05 mg/L [4]. Because chromium could easily penetrate the cell wall, it was a carcinogenic, mutagenic, acutely toxic and teratogenic element for most living organisms of human, plants and animals [5,6]. It was necessary that chromium from aqueous solution was clean up.

At present, many technologies have been reported to eliminate the chromium from aqueous solution, such as ion exchange, reverse osmosis, electrolysis, membrane filtration, chemical precipitation and adsorption [7–9]. Among these technologies, adsorption method was thought as a low cost, simple operation and high efficiency for the removal of contaminants, such as heavy metal, radionuclide, organic pollutant, inorganic pollutant, and so on [10,11]. However, some of the reported adsorbents for the removal of chromium also have some limitations of difficult filtration, easy agglomeration or low adsorption capacities [12–14].

---

* Corresponding author.

Therefore, the development of high efficiency, low cost and good chemical stability adsorbents for removing chromium from aqueous solution was very urgent.

In recent years, biochars have been attracted attention owing to their low cost, high carbon content, high surface area, natural biomass, performance in the treatment of environmental pollutants [15–17]. Biochars were pyrogenic carbon material produced by the rich carbon materials (such as, forestry waste, agricultural straw, animal manure, etc.) under oxygen-limited environment. They are adsorption materials of porous irregular structures, high surface area, lower cost, controllable chemical characteristic [18,19]. Therefore, they could successfully be applied into the eliminating of environmental pollutants [20]. However, application of biochar was limited due to their small particle size and low density [21]. In order to enhance their performance, various modification methods have been elaborated in details [22]. Zhang et al. [23] reported that the mechanism of decrease in As bioavailability after addition of FMCBC to As-contaminated soil. It could prevent heavy metal denaturation and improve soil enzyme heavy metal tolerance. Sun et al. [24] found that biochar could be supported by the survival of *Bacillus mucilaginosus*. The modified BC from corn stalk could adsorb more volatile organic compounds compared with rice straw under mushroom medium. BC modified by nano-Mn oxide exhibited good performance of oxytetracycline and DBP removal. It also could imply that the combination of BC and nano-Mn oxide improved the adsorption capacity [25].

Recently, $MeFe_2O_4$ nanoparticles (Me represented the element of Mg, Mn, Cu, Ni, Co, etc.) was recognized as adsorption material containing of magnetic permeability, high performance and chemical stability, which have been widely researched on the removal of the heavy metals from aqueous solution [26–28]. Among the $MeFe_2O_4$ nanoparticles, $MnFe_2O_4$ nanoparticles were thought as a good performance adsorbent because of their high potential of ion binding, small specific surface area and large number of active functional groups. Additionally, the application of $MnFe_2O_4$ nanoparticles exhibited no toxicity effect for environment [29]. It indicated it could be used for high efficiency removal capacity of toxic heavy metals ions from aqueous solution. However, $MnFe_2O_4$ nanoparticles were easy to be agglomerated and decreased their activity and chemical stability. If $MnFe_2O_4$ nanoparticles were combined with biochar, it could be compensated each other in terms of practical application shortcomings. $MnFe_2O_4$ nanoparticles could transfer its characteristics of high potential of ion binding, small specific surface area and large number of active functional groups to biochar. Furthermore, biochar could provide a high performance platform to prevent the agglomeration of $MnFe_2O_4$ nanoparticles. Therefore, the combination of biochar with $MnFe_2O_4$ nanoparticles not only could compensate their shortcoming, but also could develop the adsorption material of the biochar and $MnFe_2O_4$ nanoparticles.

In this research, the removal capacity of Cr(VI) by the preparation of porous biochar decorated with $MnFe_2O_4$ magnetic nanoparticle ($MnFe_2O_4$@PS) was evaluated. The main objectives were following: (1) characterization of $MnFe_2O_4$@PS; (2) adsorption process of Cr(VI) by $MnFe_2O_4$@PS; (3) adsorption mechanism of Cr(VI) by $MnFe_2O_4$@PS; (4) chemical stability of $MnFe_2O_4$@PS.

2. Experimental

2.1. Materials

Chemical agents in this experiment all were analytical grade and without further purification. The double distilled water was used in this experiment. Ferric nitrate ($Fe(NO)_3{\cdot}9H_2O$), manganese nitrate ($Mn(NO_3)_2{\cdot}4H_2O$), potassium dichromate ($K_2Cr_2O_7$), sodium hydroxide (NaOH), sulfuric acid (H_2SO_4) and hydrochloric acid (HCl) were purchased from Shanghai Macleans Chemical Reagent Co., Ltd. (Shanghai, P.R. China). Peanut shells were obtained from local farm (Shaoxing, P.R. China).

2.2. Preparation of $MnFe_2O_4$@PS

The biochar from peanut shell (PS) was prepared by high temperature hydrothermal method. Briefly, peanut shell was washed for several times with double distilled water in order to remove the dust and impurities on the surface of peanut shell. The washed peanut shells were dried at 65°C for 24 h. Then 5 g of the dried peanut shells were grounded into 80 meshes, and mixed with 20 mL of double distilled water. The mixture solution was stirred for 20 min under magnetic stirrer, and heated at 150°C for 24 h under steam pressure cooker. Cooled at room temperature, the obtained black powder was dried at 105°C for 6 h.

The adsorbent of $MnFe_2O_4$@PS composite material was developed by co-precipitation method. In a word, 4.0 g of PS was added into 250 mL Erlenmeyer flask containing the 50 mL mixture solution of 0.4 mol/L Mn^{2+} solution and 0.4 mol/L Fe^{3+} solution. Then, the mixture solution was stirred for 10 min under magnetic stirrer. 50 mL 1.0 mol/L NaOH was slowly dropped into the flask, and stirred for 20 min again under magnetic stirrer. Filtered with filter paper, and dried at 105°C for 12 h. The synthesis pathway for $MnFe_2O_4$@PS composites is shown in Fig. 1.

2.3. Characterization of $MnFe_2O_4$@PS

$MnFe_2O_4$@PS and PS were characterized by scanning electron microscopy (SEM), transmission electron microscopy (TEM), X-ray diffraction (XRD), Fourier-transform infrared spectroscopy (FT-IR) and X-ray photoelectron spectroscopy (XPS), respectively. The details of these analytical techniques were shown in Supporting Information.

2.4. Adsorption experiments

The Cr(VI) ions removal experiments by $MnFe_2O_4$@PS composites were carried out in 250 mL Erlenmeyer flask at 200 rpm and constant temperature. Briefly, $MnFe_2O_4$@PS composites were added into 250 mL Erlenmeyer flask containing 100 mL Cr(VI) ions. The initial pH in solution was adjusted with 0.1 mol/L NaOH or 0.1 mol/L HCl. The flask was placed in a shaker at 200 rpm and constant temperature. The sample was centrifuged at 5,000 rpm for 15 min. The supernatant was passed 0.25 um filter, and

Fig. 1. Synthesis pathway for $MnFe_2O_4$@PS composites.

the concentration of Cr(VI) was determined by Flame Atomic Absorption Spectrophotometer (FAAS). The residual sample was characterized by spectrum technology. All experiments were carried out for three times, and the experimental data were analyzed by the mean and standard deviation. Additionally, calculation equations of the uptake capacity (*q* (mg/g)) and the removal rate (*R* (%)) were provided in Supporting Information. The detail of adsorption experiments (effect of contact time, initial concentration of Cr(VI), initial pH in solution and temperature) and regeneration experiment also were described in the Supporting Information.

3. Results and discussion

3.1. Characterization

The Brunauer–Emmett–Teller (BET) and pore width of PS and $MnFe_2O_4$@PS are determined by NOVA 4200e Surface Area and Pore Size Analyzer. The BET of PS and $MnFe_2O_4$@PS are 25.43 and 54.65 m^2/g respectively. The average pore width of PS and $MnFe_2O_4$@PS are 5.5 and 18.7 nm respectively. The BET and pore width of PS modified by $MnFe_2O_4$ nanoparticles are increased. It indicates that the $MnFe_2O_4$ nanoparticles are loaded onto the surface of PS successfully. The morphologies of PS and $MnFe_2O_4$@PS composites could be observed by SEM and TEM, which are shown in Fig. 2.

It could be found that the micrograph of PS was entirely different with that of PS. It could be concluded that $MnFe_2O_4$@PS composites were combined with PS in

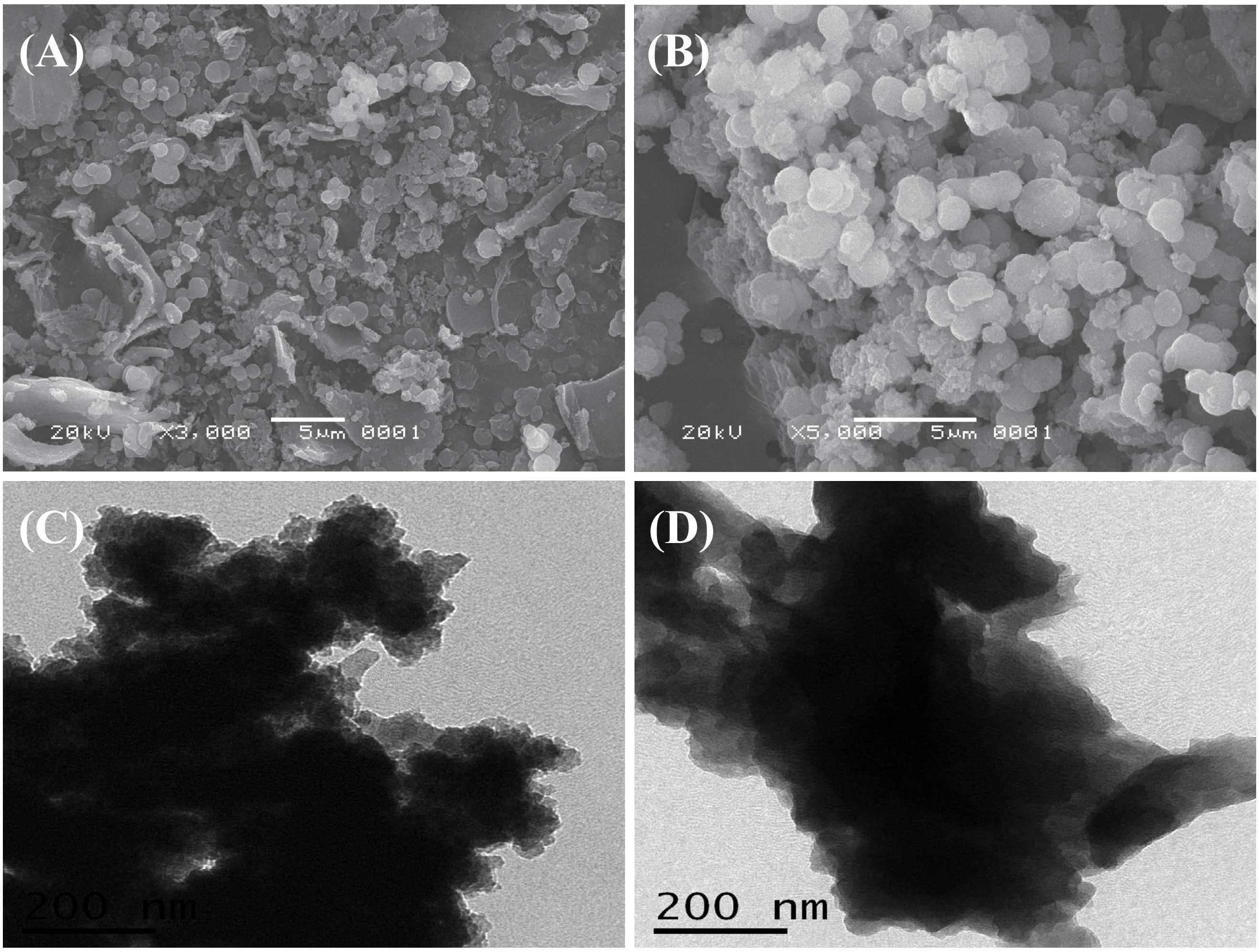

Fig. 2. SEM images of PS (A), $MnFe_2O_4$@PS composites (B), TEM images of PS (C) and $MnFe_2O_4$@PS composites (D).

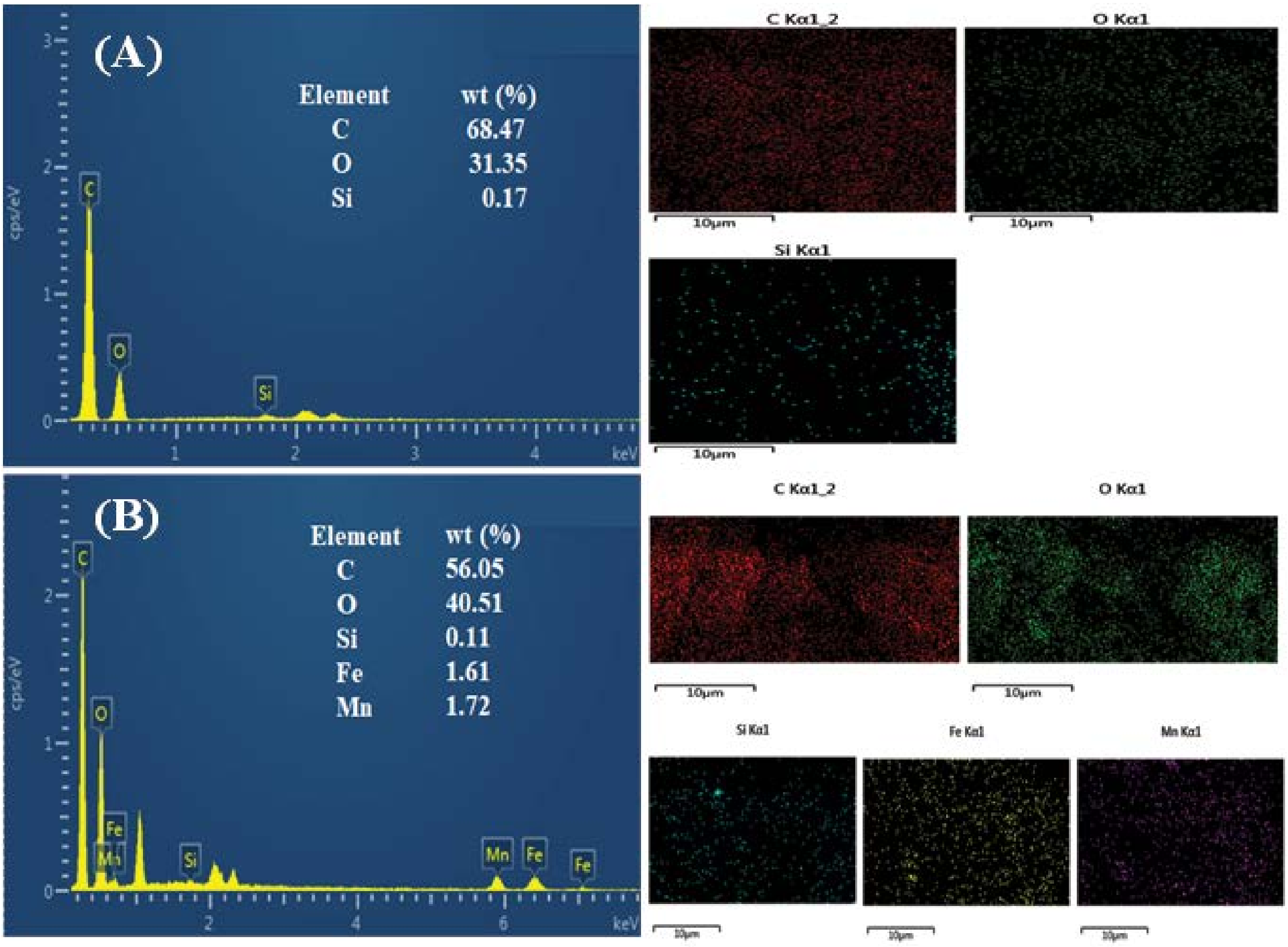

Fig. 3. EDS spectrum and elemental mapping images of PS (A) and MnFe$_2$O$_4$@PS composites (B).

this work. The micrograph of PS (Fig. 2A and C) showed that there were the large amounts of irregular particles on the surface of PS, and their surface was smooth. As shown from the micrograph of MnFe$_2$O$_4$@PS composites (Fig. 2B and D), it could be observed that large amounts of rough and irregular nanoparticles were appeared on the surface of PS. It also indicated that the combination of PS and MnFe$_2$O$_4$@PS composites could slow down the agglomeration of MnFe$_2$O$_4$@PS composites [30].

Energy-dispersive X-ray (EDS) spectrum and elemental mapping images of PS and MnFe$_2$O$_4$@PS composites are displayed in Fig. 3.

As shown in Fig. 3, the elements of PS contained C, O and Si. Their wt.(%) were 68.47%, 31.35% and 0.17%, respectively. After MnFe$_2$O$_4$ magnetic nanoparticle loading, the elements were C, O, Si, Fe and Mn, respectively. Their wt.(%) were 56.05, 40.51, 0.11, 1.61 and 1.72%, respectively. It could be observed that the relative contents of oxygen increased evidently. This might indicate that Mn–O–C and Fe–O–C were appeared on the surface of MnFe$_2$O$_4$@PS composites [31]. It also confirmed again that MnFe$_2$O$_4$ magnetic nanoparticle was successfully loaded on the surface of PS. The results were consistent with the results of SEM and TEM.

In order to evaluate the characterization of PS and MnFe$_2$O$_4$@PS composites, they also were characterized by FT-IR, XRD and XPS, respectively (Fig. 4).

FT-IR spectrum of PS and MnFe$_2$O$_4$@PS are displayed in Fig. 4A. For PS and MnFe$_2$O$_4$@PS, five characteristic peaks at 3,390; 2,332; 1,610; 1,379 and 598 cm^{-1} were observed. They were attributed to the stretching vibration of O–H, stretching vibration of C–H, stretching vibration of C=C, stretching vibration of C–O and stretching of organic matters, respectively [32–35]. For MnFe$_2$O$_4$@PS, the characteristic peak at 598 cm^{-1} appeared, and it was attributed to the stretching vibration of Fe–O and Mn–O [36]. Furthermore, compared with PS, transmittance of bands for MnFe$_2$O$_4$@PS observably changed. It indicated that the interaction between PS and MnFe$_2$O$_4$ nanoparticles appeared. It also was confirmed that MnFe$_2$O$_4$ nanoparticles and PS were successfully combined.

XRD patterns of PS and MnFe$_2$O$_4$@PS were shown in Fig. 4B. For PS, the diffraction peak at 26.62° was confirmed as quartz (SiO$_2$). It also was the main component of PS. For MnFe$_2$O$_4$@PS, the diffraction peaks at 25.94°, 31.12° and 34.2° could be confirmed as jacobsite (MnFe$_2$O$_4$). It indicated the successful preparation of MnFe$_2$O$_4$@PS composites. XPS spectra of MnFe$_2$O$_4$@PS were depicted in

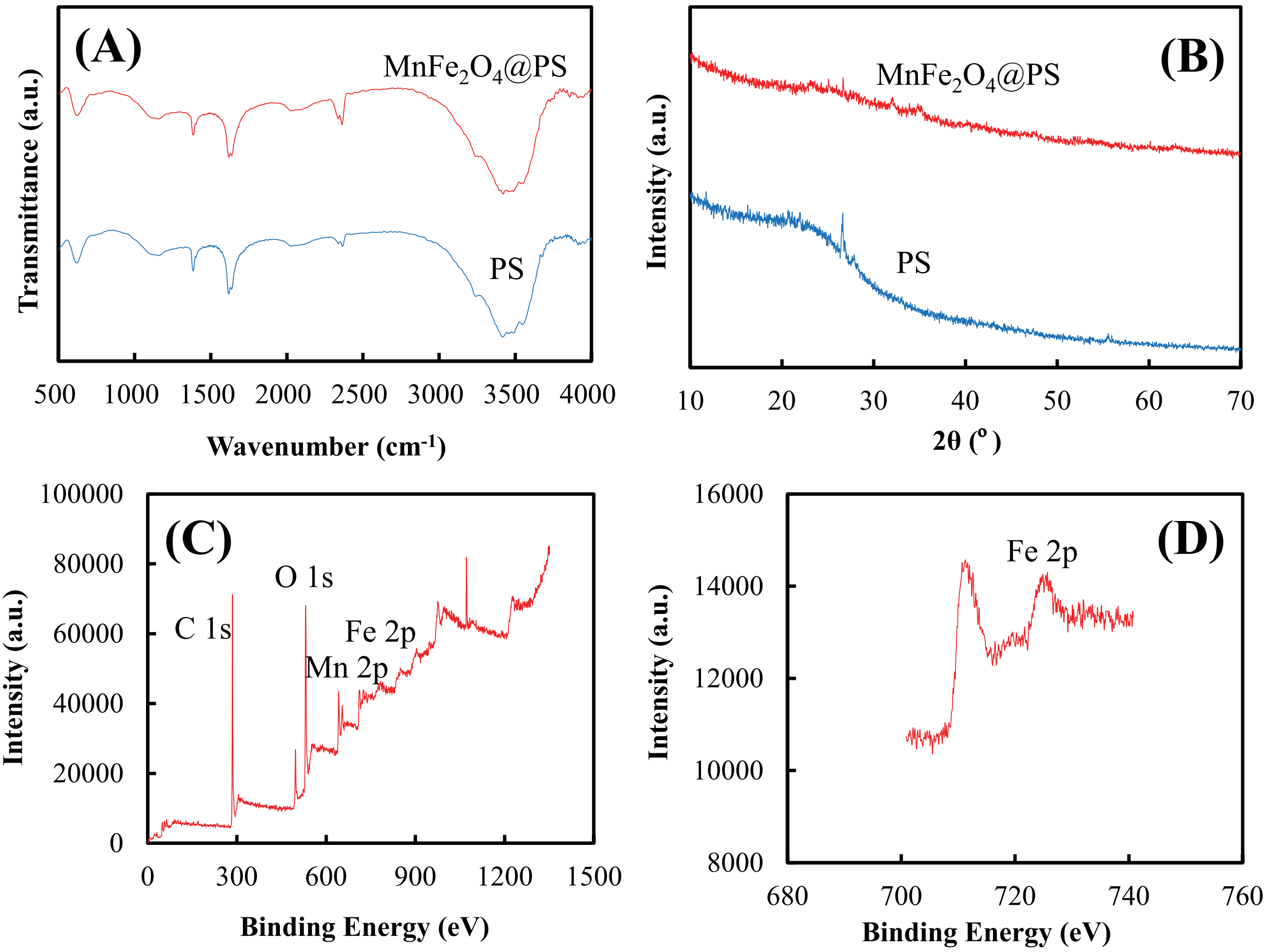

Fig. 4. FT-IR spectrum of PS and MnFe$_2$O$_4$@PS (A), XRD patterns of PS and MnFe$_2$O$_4$@PS (B), XPS spectra of MnFe$_2$O$_4$@PS, (C) survey scan and (D) Fe 2p.

Fig. 4C and D. As shown from Fig. 4C, two new peaks of binding energy appeared at 641.65 and 711.12 eV, which could be contributed as Mn 2p photoelectron and Fe 2p photoelectron. Additionally, Fe 2p spectrum indicated that two characteristic peaks at 711.98 and 726.28 eV should be Fe 2p$_{3/2}$ and Fe 2p$_{1/2}$. It implied that the formation of Fe on the surface of MnFe$_2$O$_4$@PS was Fe(III). It also confirmed that PS was successfully combined with MnFe$_2$O$_4$ nanoparticles. This result was consistent with the results of SEM, TEM, EDS, FT-IR and XRD.

3.2. Effect of operation parameters

In order to evaluate effect of operation parameters on Cr(VI) removal by MnFe$_2$O$_4$@PS, the adsorption experiments were carried out. The details of adsorption experiments were depicted in Supporting Information. The experimental results were shown in Fig. 5. From Fig. 5A, the initial pH in solution had an important influence on Cr(VI) removal. Along with the increasing of pH from 2.0 to 12.0, removal capacity of Cr(VI) ions in solution decreased drastically. The main reasons should be connected with Cr(VI) species in different pH in solution. When pH < 6.0, $HCrO_4^-$ ions were the predominant ion species in solution. However, when pH > 6.0, CrO_4^{2-} ions were the predominant ion species in solution [3]. Cr(VI) ions in solution could be removed by MnFe$_2$O$_4$@PS composites through the electrostatic interaction. At lower pH, the anionic species appeared on the surface of MnFe$_2$O$_4$@PS composites. Therefore, the removal capacity of Cr(VI) ions by MnFe$_2$O$_4$@PS composites was high [8,37]. However, along with the increase of the initial pH in solution, the charge on the surface of MnFe$_2$O$_4$@PS composites become more negative. Thus, the removal capacity of Cr(VI) ions by MnFe$_2$O$_4$@PS composites decreased because of the presence of CrO_4^{2-} ions as the predominant ion species. It also could be implied that the removal mechanism of Cr(VI) ions by MnFe$_2$O$_4$@PS composites should contain the electrostatic interaction. Fig. 5B showed the effect of reaction time on the removal capacity of Cr(VI) ions by MnFe$_2$O$_4$@PS composites. The removal capacity of Cr(VI) ions by MnFe$_2$O$_4$@PS composites increased sharply at the first 30 min. Then, the removal capacity of Cr(VI) ions by MnFe$_2$O$_4$@PS composites begun to increase slowly, and it reached equilibrium about 300 min. It might be the reasons

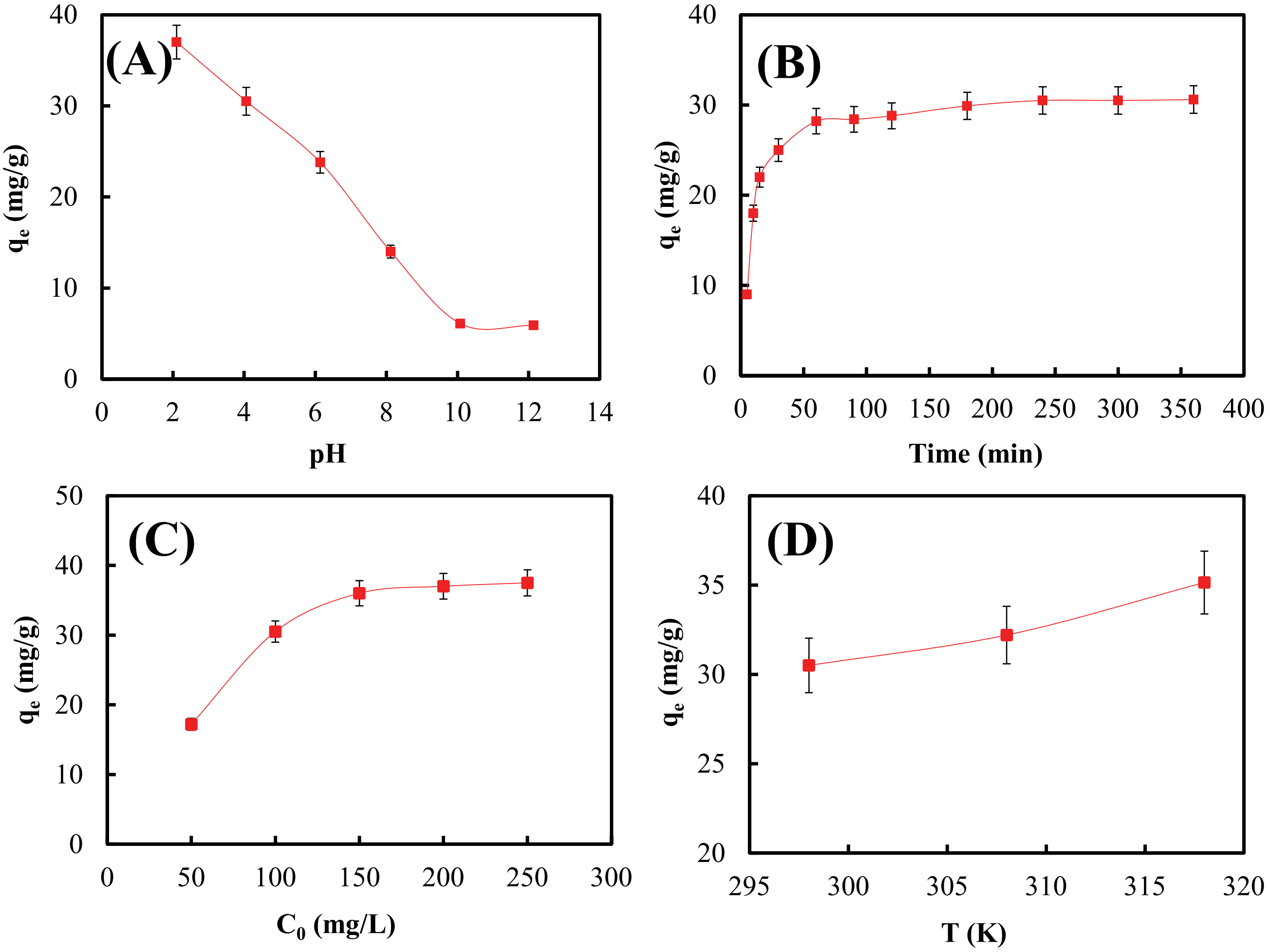

Fig. 5. Effect of operation parameters on removal capacity of Cr(VI) by $MnFe_2O_4$@PS (Reaction conditions: 0.1 g adsorbent; 100 mg/L Cr(VI); pH 4.0; 200 rpm; 25°C for 8 h).

that the sufficient number of adsorption sites on the surface of $MnFe_2O_4$@PS composites appeared at the beginning of adsorption process. Then, along with the development of adsorption process, adsorption sites on the surface of $MnFe_2O_4$@PS composites decreased slowly. This leaded to the decrease of removal capacity of Cr(VI) ions. Effect of initial concentration of Cr(VI) and reaction temperature on removal capacity of Cr(VI) are shown in Fig. 5C and D, respectively. It could be observed that the increase of initial concentration of Cr(VI) and reaction temperature would contribute to the adsorption process of Cr(VI) removal by $MnFe_2O_4$@PS composites.

3.3. Adsorption kinetic, adsorption isotherm and thermodynamic

To elaborate the mechanism of Cr(VI) removal by $MnFe_2O_4$@PS composites, adsorption kinetic, adsorption isotherm and thermodynamic were discussed in details. In this research, pseudo-first-order, pseudo-second-order, Langmuir and Freundlich models were used to elaborate the adsorption behavior of Cr(VI) ions on $MnFe_2O_4$@PS composites. Their equations and the calculation of thermodynamic parameters were shown in Supporting Information.

According to the experimental results of Fig. 5B, the adsorption kinetic for Cr(VI) removal by $MnFe_2O_4$@PS composites were shown in Fig. 6A and B.

It could be observed that the value of R^2 for pseudo-second-order model was higher than that of R^2 for pseudo-first-order model (0.9998 > 0.9495). It also indicated that the main adsorption process was chemisorption [38]. According to the experimental results of Fig. 5C, the adsorption isotherm for Cr(VI) removal by $MnFe_2O_4$@PS composites were shown in Fig. 6C and D. As shown in Fig. 6C and D, the Langmuir model could be used to describe the adsorption process according to its higher value of R^2 (0.9824 > 0.8658). According to the Langmuir model, the theoretical q_m could be calculated. The value of q_m reached 46.51 mg/g. It exhibited high removal capacity of Cr(VI) by $MnFe_2O_4$@PS composites. Additionally, it also implied that the adsorption process of Cr(VI) ions by $MnFe_2O_4$@PS composites was monolayer adsorption [39].

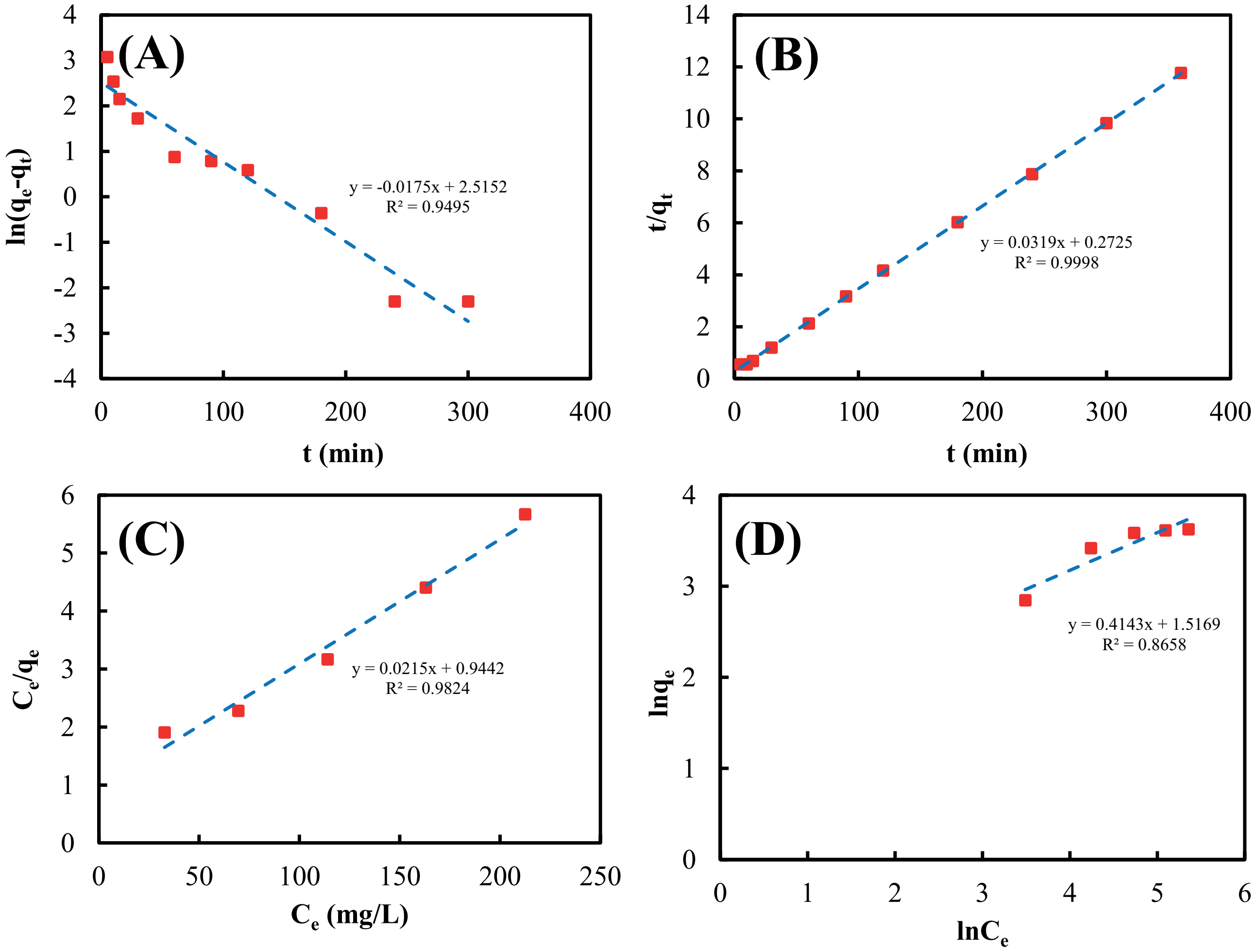

Fig. 6. Adsorption kinetic and the adsorption isotherm for Cr(VI) removal by $MnFe_2O_4$@PS composites (A) pseudo-first-order, (B) pseudo-second-order, (C) Langmuir and (D) Freundlich.

According to the experimental results of Fig. 5D, the thermodynamic values could be calculated, and were listed in Table S1. The positive values of $\Delta H°$ and $\Delta S°$ indicated that the removal of Cr(VI) ion by $MnFe_2O_4$@PS composites was the endothermic and randomness process, respectively. Additionally, the negative values of $\Delta G°$ revealed that the adsorption process also was a spontaneous process. The increase of reaction temperature would lead to the greater adsorption driving force and improve the adsorption of Cr(VI) by $MnFe_2O_4$@PS composites. In a word, the adsorption process of Cr(VI) by $MnFe_2O_4$@PS composites was a spontaneous, endothermic and randomness process.

3.4. Adsorption mechanism

In order to elaborate the adsorption mechanism of Cr(VI) removal by $MnFe_2O_4$@PS composites, $MnFe_2O_4$@PS composites were determined by many technologies. According to the results of SEM and TEM, $MnFe_2O_4$@PS composite was a pore, rough and irregular structure. It was benefit for removal of Cr(VI) through physical adsorption. Additionally, the large number of functional groups (such as O–H, C–H, C=C, C–O, and so on) were observed on the surface of $MnFe_2O_4$@PS composite. Therefore, they could react with Cr(VI) ions by electrostatic surface complexation and cationic attraction [34]. Additionally, $MnFe_2O_4$@PS composites after adsorption of Cr(VI) also were determined by XPS technology. The results of XPS were depicted in Fig. 7.

The survey of XPS spectrum was shown in Fig. 7A. The elements of the $MnFe_2O_4$@PS composites could be observed. Before adsorption of Cr(VI), the peaks at 284.86, 531.07, 641.65 and 711.12 eV were corresponding to C 1s, O 1s, Mn 2p and Fe 2p species, respectively. Additionally, their atomic were 61.88%, 31.37%, 3.34% and 3.41%, respectively. After adsorption of Cr(VI), the new peak at 582.12 eV appeared. It was corresponding to Cr 2p species. It indicated that Cr(VI) ions in solution could be adsorbed by $MnFe_2O_4$@PS composites. Fig. 7D–E depicted the high resolution XPS spectrum of Fe 2p and Mn 2p. XPS spectrum of Fe 2p contained two characteristic peaks at 711.98 and 726.28 eV corresponding to Fe $2p_{3/2}$ and Fe $2p_{1/2}$ states, respectively.

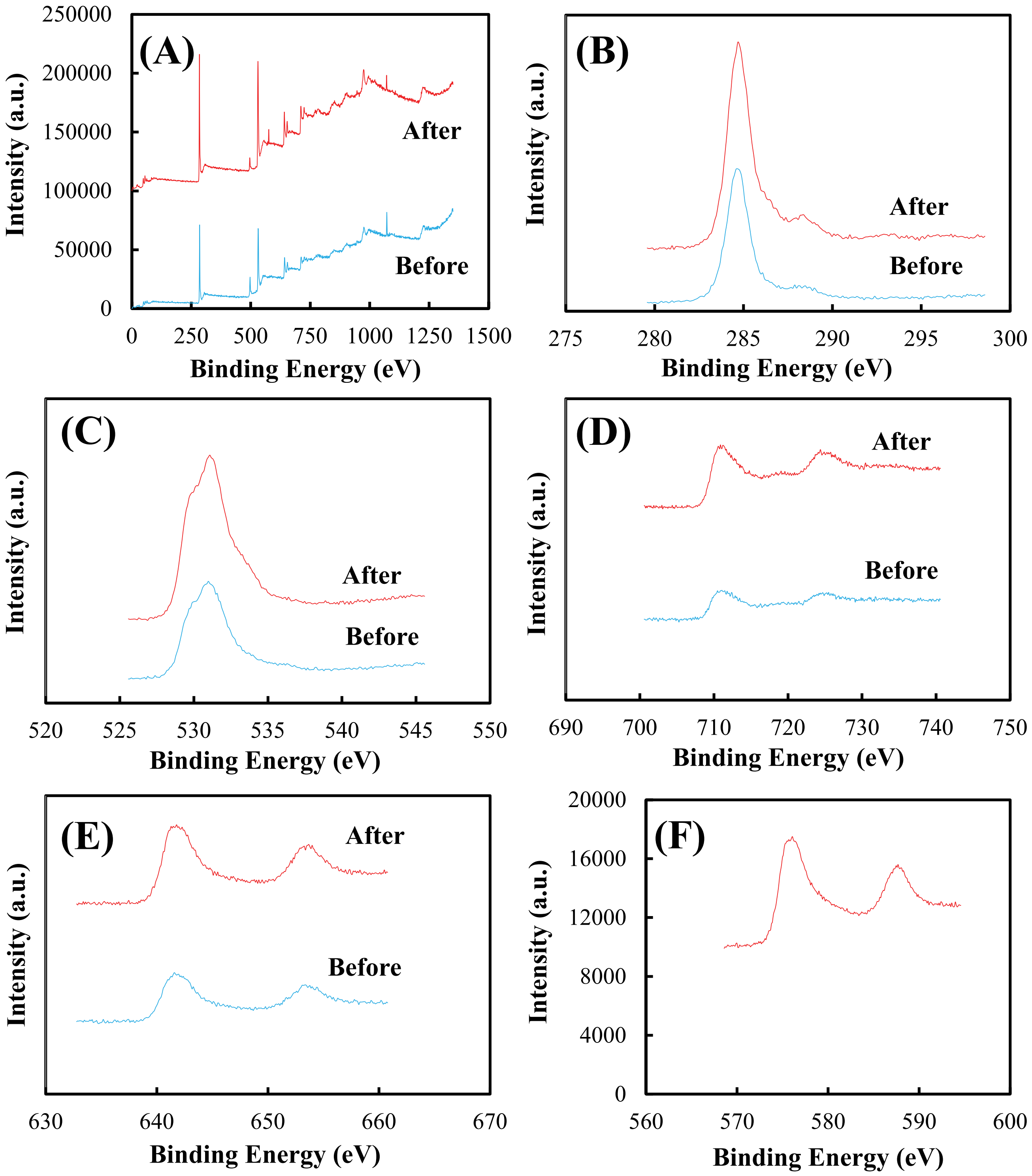

Fig. 7. XPS spectra of $MnFe_2O_4$@PS composites and $MnFe_2O_4$@PS-Cr composites (A) survey, (B) C 1s, (C) O 1s, (D) Fe 2p, (E) Mn 2p and (F) Cr 2p.

Additionally, XPS spectrum of Mn 2p contained two characteristic peaks at 642.18 and 653.98 eV corresponding to Mn $2p_{3/2}$ and Mn $2p_{1/2}$ states, respectively. It could confirm the Mn^{2+} oxidation state of Mn element. From Fig. 7B and C, it indicated that O–H, C–H, C=C and C–O could be observed on the surface of $MnFe_2O_4$@PS composites.

The proportion of functional groups on the surface of $MnFe_2O_4$@PS composites before and after adsorption exhibited an obvious change, which indicated that these functional groups reacted with Cr(VI) ions in solution. According to the above experimental results, it could be concluded that adsorption of Cr(VI) by $MnFe_2O_4$@PS composites could be attributed to the combination of chemisorption and physisorption. From the effect of pH in solution on adsorption, it could be found that Cr(VI) ions in solution could be removed by $MnFe_2O_4$@PS composites through the electrostatic interaction and chemical precipitation. At high pH, Cr(VI) reacted with OH^-, and the precipitation were formed. Additionally, Cr(VI) ions in solution could react with –OH functional groups on the surface of $MnFe_2O_4$@PS composites. The reaction was following: $MnFe_2O_4@PS\text{-}OH + Cr^{6+} \rightarrow MnFe_2O_4@PS\text{-}O^-\text{-}Cr^{6+} + H^+$. Additionally, van der Waals force played an important role between Cr(VI) and the porous material of $MnFe_2O_4$@PS composites. It could adsorb Cr(VI) through electrostatic attraction, surface adsorption and surface complexation.

Therefore, according to the results of XPS technology and the characterization of $MnFe_2O_4$@PS composites, the possible mechanism of Cr(VI) removal by $MnFe_2O_4$@PS composites was suggested. They were shown in Fig. 8.

The adsorption of Cr(VI) by $MnFe_2O_4$@PS composites could be attributed to the combination of chemisorption and physisorption. The main mechanisms contained electrostatic interaction, surface adsorption, surface complexation and chemical precipitation.

3.5. Regeneration experiment

The regeneration experiments were carried out. That is, 100 mg adsorbent and 100 mL 100 mg/L Cr(VI) ions in solution were charged into a series of flasks, respectively. The mixture was shaken at pH 4.0, 200 rpm and 25°C for 360 min. Then, concentration of Cr(VI) in solution was determined by FAAS and $MnFe_2O_4$@PS composites were washed by (1 + 1) hydrochloric acid for three times. The regeneration experiments were performed with five times. The experimental results were depicted in Fig. 9.

After five times, the removal rate of Cr(VI) ions in solution by $MnFe_2O_4$@PS composites decreased from 30.5% to 26.4%. It indicated that $MnFe_2O_4$@PS composites could be

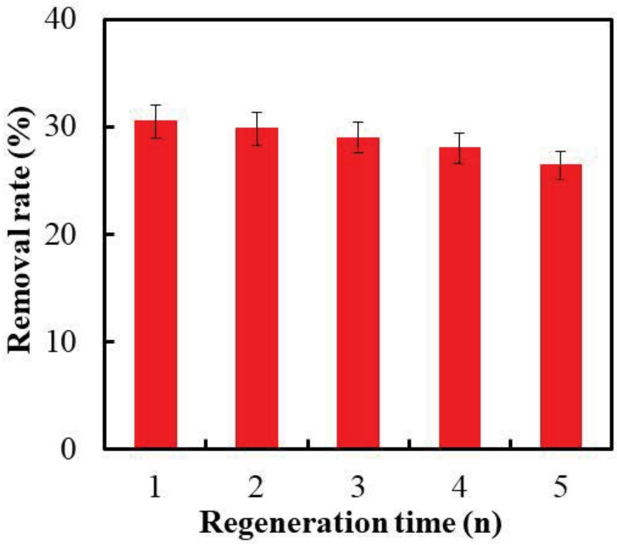

Fig. 9. Effect of regeneration time on removal rate of Cr(VI) ions in solution by $MnFe_2O_4$@PS composites (Reaction conditions: 0.1 g adsorbent; 100 mg/L Cr(VI); pH 4.0; 200 rpm; 25°C for 360 min).

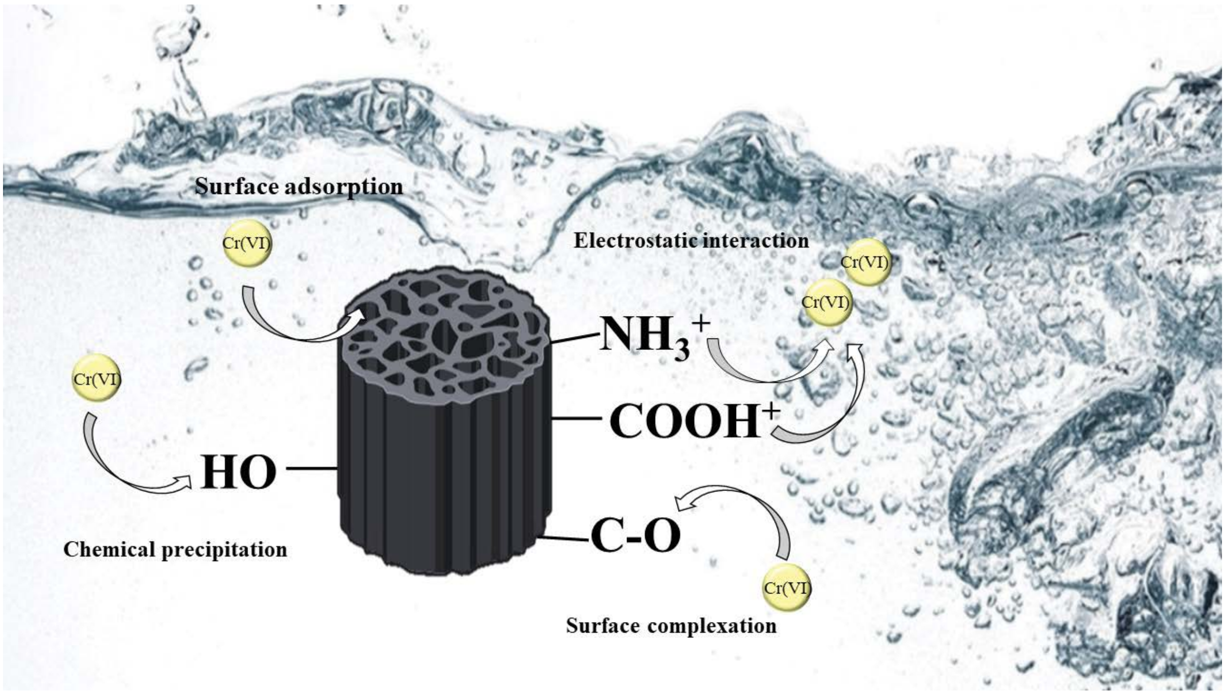

Fig. 8. The possible adsorption mechanism.

reused for removal of Cr(VI) ions in solution. The chemical stability and recyclability of $MnFe_2O_4$@PS composites was good.

4. Conclusions

In this research, the adsorbent of $MnFe_2O_4$@PS composite material was developed by co-precipitation method. $MnFe_2O_4$@PS composites were characterized by SEM, TEM, XRD, FT-IR and XPS, respectively. $MnFe_2O_4$ nanoparticles and PS were successfully combined. A lot of functional groups (such as O–H, C–H, C=C, C–O and stretching of organic matters) were observed on the surface of $MnFe_2O_4$@PS composites. The adsorption process could be described by pseudo-second-order model and Langmuir model. It also indicated that the main adsorption process was chemisorption and monolayer adsorption. The value of q_m would reach 46.51 mg/g. The adsorption process of Cr(VI) by $MnFe_2O_4$@PS composites was a spontaneous, endothermic and randomness process. The main mechanisms contained electrostatic interaction, surface complexation and chemical precipitation. The chemical stability and recyclability of $MnFe_2O_4$@PS composites for Cr(VI) removal were good.

Conflicts of interest

There are no conflicts of interest to declare.

Acknowledgements

This work is supported by the Natural Science Foundation of Zhejiang Province, China (LGF20C030001). Authors are very grateful for their support.

References

[1] F. Ge, M.-M. Li, H. Ye, B.-X. Zhao, Effective removal of heavy metal ions Cd^{2+}, Zn^{2+}, Pb^{2+}, Cu^{2+} from aqueous solution by polymer-modified magnetic nanoparticles, J. Hazard. Mater., 211–212 (2012) 366–372.

[2] Y. Zhu, X. He, J. Xu, Z. Fu, S. Wu, J. Ni, B. Hu, Insight into efficient removal of Cr(VI) by magnetite immobilized with *Lysinibacillus* sp. JLT12: mechanism and performance, Chemosphere, 262 (2021) 127901, doi: 10.1016/j.chemosphere.2020.127901.

[3] B. Eyvazi, A. Jamshidi-Zanjani, A.K. Darban, Synthesis of nanomagnetic $MnFe_2O_4$ to remove Cr(III) and Cr(VI) from aqueous solution: a comprehensive study, Environ. Pollut., 265 (2020) 113685, doi: 10.1016/j.envpol.2019.113685.

[4] M. Ghanbarian, R. Nabizadeh, S. Nasseri, F. Shemirani, A.H. Mahvi, M.H. Beyki, A. Mesdaghinia, Potential of amino-riched nano-structured $MnFe_2O_4$@cellulose for biosorption of toxic Cr(VI): modeling, kinetic, equilibrium and comparing studies, Int. J. Biol. Macromol., 104 (2017) 465–480.

[5] Y. Wang, Z. Fang, Y. Kang, E.P. Tsang, Immobilization and phytotoxicity of chromium in contaminated soil remediated by CMC-stabilized nZVI, J. Hazard. Mater., 275 (2014) 230–237.

[6] R. Liu, H. Wang, L. Han, B. Hu, M. Qiu, Reductive and adsorptive elimination of U(VI) ions in aqueous solution by SFeS@biochar composites, Environ. Sci. Pollut. Res. Int., 28 (2021) 55176–55185.

[7] Y.A. El-Taweel, E.M. Nassef, I. Elkheriany, D. Sayed, Removal of Cr(VI) ions from waste water by electrocoagulation using iron electrode, Egypt. J. Pet., 24 (2015) 183–192.

[8] F. Liu, S. Hua, C. Wang, M. Qiu, L. Jin, B. Hu, Adsorption and reduction of Cr(VI) from aqueous solution using cost-effective caffeic acid functionalized corn starch, Chemosphere, 2021 (279) 130539, doi: 10.1016/j.chemosphere.2021.130539.

[9] M. Qiu, B. Hu, Z. Chen, H. Yang, L. Zhuang, X. Wang, Challenges of organic pollutant photocatalysis by biochar-based catalysts, Biochar, 3 (2021) 117–123.

[10] Q. Lia, Z. Chen, H. Wang, H. Yang, T. Wen, S. Wang, B. Hu, X. Wang, Removal of organic compounds by nanoscale zero-valent iron and its composites, Sci. Total Environ., 792 (2021) 148546, doi: 10.1016/j.scitotenv.2021.148546.

[11] M. Qiu, Z. Liu, S. Wang, B. Hu, The photocatalytic reduction of U(VI) into U(IV) by ZIF-8/g-C_3N_4 composites at visible light, Environ. Res., 196 (2021) 110349, doi: 10.1016/j.envres.2020.110349.

[12] D. Huang, G. Wang, Z. Shi, Z. Li, F. Kang, F. Liu, Removal of hexavalent chromium in natural groundwater using activated carbon and cast iron combined system, J. Cleaner Prod., 165 (2017) 667–676.

[13] G. Vilardi, J.M. Ochando-Pulido, N. Verdone, M. Stoller, L. Di Palma, On the removal of hexavalent chromium by olive stones coated by iron-based nanoparticles: equilibrium study and chromium recovery, J. Cleaner Prod., 190 (2018) 200–210.

[14] H. Wang, R.R. Liu, H.F. Wang, B.W. Hu, M.Q. Qiu, High effective enrichment of U(VI) from aqueous solutions on versatile crystalline carbohydrate polymer-functionalized graphene oxide, Dalton Trans., 50 (2021) 14009–14017.

[15] F. Wang, L.-Y. Liu, F. Liu, L.-G. Wang, T. Ouyang, C.-T. Chang, Facile one-step synthesis of magnetically modified biochar with enhanced removal capacity for hexavalent chromium from aqueous solution, J. Taiwan Inst. Chem. Eng., 81 (2017) 414–418.

[16] E.-B. Son, K.-M. Poo, H.O. Mohamed, Y.-J. Choi, W.-C. Cho, K.-J. Chae, A novel approach to developing a reusable marine macro-algae adsorbent with chitosan and ferric oxide for simultaneous efficient heavy metal removal and easy magnetic separation, Bioresour. Technol., 259 (2018) 381–387.

[17] R. Singh, D.V. Naik, R.K. Dutta, P.K. Kanaujia, Biochars for the removal of naphthenic acids from water: a prospective approach towards remediation of petroleum refinery wastewater, J. Cleaner Prod., 266 (2020) 121986, doi: 10.1016/j.jclepro.2020.121986.

[18] B. Hu, Y. Ai, J. Jin, T. Hayat, A. Alsaedi, L. Zhuang, X. Wang, Efficient elimination of organic and inorganic pollutants by biochar-based materials, Biochar, 2 (2020) 47–64, doi: 10.1007/s42773-020-00044-4.

[19] L. Liang, F. Xi, W. Tan, X. Meng, B. Hu, X. Wang, Review of organic and inorganic pollutants removal by biochar and biochar-based composites, Biochar, 3 (2021) 255–281.

[20] M. Qiu, L. Liu, Q. Ling, Y. Cai, S. Yu, S. Wang, D. Fu, B. Hu, X. Wang, Biochar for the removal of contaminants from soil and water: a review, Biochar, 4 (2022) 19, doi: 10.1007/s42773-022-00146-1.

[21] Z. Chen, X. He, Q. Li, H. Yang, Y. Liu, L. Wu, Z. Liu, B. Hu, X. Wang, Low-temperature plasma induced phosphate groups onto coffee residue-derived porous carbon for efficient U(VI) extraction, J. Environ. Sci., 122 (2022) 1–13, doi: 10.1016/j.jes.2021.10.003.

[22] S. Yu, H. Tang, D. Zhang, S. Wang, M. Qiu, G. Song, D. Fu, B. Hu, X. Wang, MXenes as emerging nanomaterials in water purification and environmental remediation, Sci. Total Environ., 811 (2022) 152280, doi: 10.1016/j.scitotenv.2021.152280.

[23] G.G. Zhang, X.W. Liu, M.L. Gao, Z.G. Song, Effect of Fe-Mn-Ce modified biochar composite on microbial diversity and properties of arsenic-contaminated paddy soils, Chemosphere, 250 (2020) 126249, doi: 10.1016/j.chemosphere.2020.126249.

[24] D.Q. Sun, J. Meng, H. Liang, E. Yang, Y.W. Huang, W.F. Chen, L.L. Jiang, Y. Lan, W.M. Zhang, J.P. Gao, Effect of volatile organic compounds absorbed to fresh biochar on survival of *Bacillus mucilaginosus* and structure of soil microbial communities, J. Soils Sediments, 15 (2015) 271–281.

[25] M.L. Gao, Y. Zhang, X.L. Gong, Z.G. Song, Z.Y. Guo, Removal mechanism of di-n-butyl phthalate and oxytetracycline from aqueous solutions by nano-manganese dioxide modified biochar, Environ. Sci. Pollut. Res., 25 (2018) 7796–7807.

[26] N. Ueda Yamaguchi, R. Bergamasco, S. Hamoudi, Magnetic $MnFe_2O_4$–graphene hybrid composite for efficient removal of glyphosate from water, Chem. Eng. J., 295 (2016) 391–402.

[27] Z. Jiang, Y. Zhao, P. Yang, Formation of MFe_2O_4 (M = Co, Mn, Ni) 1D nanostructures towards rapid removal of pollutants, Mater. Chem. Phys., 214 (2018) 1–7.

[28] S. Yu, H. Pang, S. Huang, H. Tang, S. Wang, M. Qiu, Z. Chen, H. Yang, G. Song, D. Fu, B. Hu, X. Wang, Recent advances in metal-organic framework membranes for water treatment: a review, Sci. Total Environ., 800 (2021) 149662, doi: 10.1016/j.scitotenv.2021.149662.

[29] A. Mary Jacintha, V. Umapathy, P. Neeraja, S. Rex Jeya Rajkumar, Synthesis and comparative studies of $MnFe_2O_4$ nanoparticles with different natural polymers by sol–gel method: structural, morphological, optical, magnetic, catalytic and biological activities, J. Nanostruct. Chem., 7 (2017) 375–387.

[30] Y. Li, Z. Yang, H. Zhang, X. Tong, J. Feng, Fabrication of sewage sludge-derived magnetic nanocomposites as heterogeneous catalyst for persulfate activation of Orange G degradation, Colloids Surf., A, 529 (2017) 856–863.

[31] D. Ouyang, J. Yan, L. Qian, Y. Chen, L. Han, A. Su, W. Zhang, H. Ni, M. Chen, Degradation of 1,4-dioxane by biochar supported nano magnetite particles activating persulfate, Chemosphere, 184 (2017) 609–617.

[32] A.-N.A. El-Hendawy, Variation in the FT-IR spectra of a biomass under impregnation, carbonization and oxidation conditions, J. Anal. Appl. Pyrolysis, 75 (2006) 159–166.

[33] P. Devi, A.K. Saroha, Synthesis of the magnetic biochar composites for use as an adsorbent for the removal of pentachlorophenol from the effluent, Bioresour. Technol., 169 (2014) 525–531.

[34] J. Ifthikar, J. Wang, Q. Wang, T. Wang, H. Wang, A. Khan, A. Jawad, T. Sun, X. Jiao, Z. Chen, Highly efficient lead distribution by magnetic sewage sludge biochar: sorption mechanisms and bench applications, Bioresour. Technol., 238 (2017) 399–406.

[35] L. Kemmou, Z. Frontistis, J. Vakros, I.D. Manariotis, D. Mantzavinos, Degradation of antibiotic sulfamethoxazole by biochar-activated persulfate: factors affecting the activation and degradation processes, Catal. Today, 313 (2018) 128–133.

[36] K.-W. Jung, S.Y. Lee, Y.J. Lee, Facile one-pot hydrothermal synthesis of cubic spinel-type manganese ferrite/biochar composites for environmental remediation of heavy metals from aqueous solutions, Bioresour. Technol., 261 (2018) 1–9.

[37] F. Liu, S. Hua, C. Wang, B. Hu, Insight into the performance and mechanism of persimmon tannin functionalized waste paper for U(VI) and Cr(VI) removal, Chemosphere, 287 (2022) 132199, doi: 10.1016/j.chemosphere.2021.132199.

[38] A. Ngambia, J. Ifthikar, I.I. Shahib, A. Jawad, A. Shahzad, M. Zhao, J. Wang, Z. Chen, Z. Chen, Adsorptive purification of heavy metal contaminated wastewater with sewage sludge derived carbon-supported Mg(II) composite, Sci. Total Environ., 691 (2019) 306–321.

[39] S. Khandaker, Y. Toyohara, S. Kamida, T. Kuba, Effective removal of cesium from wastewater solutions using an innovative low-cost adsorbent developed from sewage sludge molten slag, J. Environ. Manage., 222 (2018) 304–315.

Supporting information

S1. Characterization of sorbents

SEM (Scanning electron microscope, JEOL 6500F, Japan) and TEM (Transmission electron microscope, Tecnai G2 20, The Netherlands) was used to observe the surface morphology and structure of adsorbents. The surface area and pore size of adsorbents were determined by the NOVA 4200e Surface Area and Pore Size Analyzer (Quantachrome, FL, USA) at a relative pressure of 0.95 following the multipoint N_2-Brunauer–Emmett–Teller adsorption method. The surface functional groups of adsorbents in the wave number range of 500–4,000 cm^{-1} were recorded on a Nexus 670 FT-IR Spectrometer (Fourier-transform infrared spectroscopy, Thermo Nicolet, Madison). The crystalline structures of the adsorbents were conducted in a D/Max-IIIA Powder X-ray Diffractomer (Rigaku Corp., Japan). XPS (X-ray photoelectron spectrometer, Kratos AXIS Ultra DLD, Japan) and the model Axis-HS (Kratos Analytical) were used to determine the surface of adsorbents.

S2. Calculation of removal rate and uptake capacity

The removal rate (R (%)) and the adsorption capacity (q (mg/g)) were calculated according to the following Eqs. (S1) and (S2).

$$R = \frac{C_0 - C_e}{C_0} \times 100\% \tag{S1}$$

$$q = \frac{\left(C_0 - C_e\right) \times V}{m} \tag{S2}$$

where C_0 (mg/L) and C_e (mg/L) are initial concentration and equilibrium concentration, respectively. V (L) is the solution volume and m (g) is the weight of adsorbent.

S3. Adsorption experiments

S3.1. Effect of pH

100 mg adsorbent and 100 mL 100 mg/L Cr(VI) ions in solution with different pH (2.0, 4.0, 6.0, 8.0, 10.0 and 12.0) were charged into a series of flasks, respectively. The mixture was shaken at 200 rpm and 25°C for 8 h.

S3.2. Effect of initial concentration

100 mg adsorbent and 100 mL initial concentration of Cr(VI) ions in solution with a different initial concentration (50, 100, 150, 200 and 250 mg/L) were charged into a series of flasks, respectively. The mixture was shaken at pH 4.0, 200 rpm and 25°C for 8 h.

S3.3. Effect of contact time

100 mg adsorbent and 100 mL 100 mg/L Cr(VI) ions in solution were charged into a series of flasks, respectively. The mixture was shaken at pH 4.0, 200 rpm and 25°C for different time (5, 10, 15, 30, 60, 90, 120, 180, 240, 300 and 360 min).

S3.4. Effect of temperature

100 mg adsorbent and 100 mL 100 mg/L Cr(VI) ions in solution were charged into a series of flasks, respectively. The mixture was shaken at pH 4.0 and 200 rpm for 8 h. Temperature is 25°C, 35°C and 45°C, respectively.

Table S1
Thermodynamic parameters of Cr(VI) ions in solution removal by $MnFe_2O_4$@PS composites

$\Delta G°$ (kJ/mol)			$\Delta H°$ (kJ/mol)	$\Delta S°$ (J/mol·K)
298 (K)	308 (K)	318 (K)		
–2.04	–1.91	–1.62	8.27	20.83

S4. Recycle experiment

100 mg adsorbent and 100 mL 100 mg/L Cr(VI) ions in solution were charged into a series of flasks, respectively. The mixture was shaken at pH 4.0, 200 rpm and 25°C for 8 h.

S4.1. Pseudo-first-order and pseudo-second-order kinetic

In order to describe the adsorption mechanism, the adsorption kinetics is described by the pseudo-first-order and pseudo-second-order kinetic models. The Eqs. (S3) and (S4) represent the linear forms of pseudo-first-order [S1] and pseudo-second-order kinetic models [S2].

$$q_t = q_e\left(1 - e^{-K_1 t}\right) \tag{S3}$$

$$\frac{t}{q_t} = \frac{1}{K_2 q_e^2} + \frac{t}{q_e} \tag{S4}$$

where q_e (mg/g) and q_t (mg/g) are adsorption capacity of Cr(VI) ions solution by $MnFe_2O_4$ magnetic nanoparticle ($MnFe_2O_4$@PS) at adsorption time t and adsorption equilibrium respectively. K_1 (min^{-1}) and K_2 (min^{-1}) are the adsorption rate constant.

S4.2. Langmuir isotherm model and Freundlich isotherm model

In order to investigate adsorption process, the experimental data of Cr(VI) uptake onto $MnFe_2O_4$@PS are analyzed using Langmuir isotherm model [S3] and Freundlich isotherm model [S4]. Langmuir isotherm model expresses monolayer adsorption. The adsorbate arrives at the unevenly surface of the adsorbent from the liquid phase. They can be expressed in Eqs. (S5) and (S6). They are following as:

$$q_e = \frac{q_m C_e K_L}{1 + C_e K_L} \tag{S5}$$

where q_e (mg/g) is concentration of adsorbed Cr(VI) ions at equilibrium. q_m (mg/g) is the maximum uptake capacity of Cr(VI). C_e (mg/L) is concentration of Cr(VI) at equilibrium and K_L (L/mg) is constant.

$$q_e = K_f C_e^{1/n} \tag{S6}$$

where q_e (mg/g) is the amount of adsorbed Cr(VI) ions per unit mass of the adsorbent at equilibrium. C_e (mg/L) is concentration of Cr(VI) ions at equilibrium. K_f and $1/n$ are constant.

S4.3. Calculation of thermodynamic parameters

In order to explore further mechanism of Cr(VI) uptake, thermodynamic parameters are evaluated to determine the spontaneity of the reaction. They are Gibbs free energy ($\Delta G°$ (kJ/mol)), enthalpy ($\Delta H°$ (kJ/mol)) and entropy ($\Delta S°$ (J/mol·K)) respectively. They are associated with the adsorption can be calculated using the following Eqs. (S7)–(S9):

$$\Delta G° = -RT \ln K_a \tag{S7}$$

$$\ln K_a = \frac{\Delta S°}{R} - \frac{\Delta H°}{RT} \tag{S8}$$

$$K_a = \frac{q_e}{C_e} \tag{S9}$$

where T is the solution temperature (K), K_a is the adsorption equilibrium constant, R is the gas constant (8.314 J/mol·K), q_e is the amount of adsorbate adsorbed per unit mass of adsorbate at equilibrium (mg/g) and C_e is the equilibrium concentration of the adsorbate (mg/L). $\Delta S°$ and $\Delta H°$ are calculated from the slope and the intercept respectively.

References

[S1] W.S. Hummers Jr., R.E. Offeman, Preparation of graphitic oxide, J. Am. Chem. Soc., 80 (1958) 1339, doi: 10.1021/ja01539a017.
[S2] S. Lagergren, Zur Theorie der sogenannten Adsorption gelöster Stoffe, Pseudo-second-order model for sorption processes, Handlingar, 24 (1898) 1–39.
[S3] I. Langmuir, The adsorption of gases on plane surfaces of glass, mica and platinum, J. Am. Chem. Soc., 40 (1918) 1361–1403.
[S4] H.M.F. Freundlich, Uber die Adsorption in Losungen, J. Phys. Chem., 57 (1906) 385–470.